Porosity, Element Loss, and Strength Model on Softening Behavior of Hybrid Laser Arc Welded Al-Zn-Mg-Cu Alloy with Synchrotron Radiation Analysis

Gas porosity and alloying elements Zn, Cu, Ti, and Mn were characterized by high-resolution synchrotron radiation analysis, and a new strength model of hybrid welded 7075-T6 joints was formulated and validated using these results

BY S. C. WU, X. YU, R. Z. ZUO, W. H. ZHANG, H. L. XIE, AND J. Z. JIANG

ABSTRACT

The severe strength loss of hybrid welded Al-Zn-Mg-Cu alloy joints such as 7075-T6 has been characterized using high-resolution synchrotron radiation X-rays and theoretical modeling. To elucidate the physical causes of this static strength change, the distribution of strengthening elements such as Zn and Cu and the three-dimensional gas porosity were mapped. The interesting findings included the following: 1) Hybrid welds only reach approximately 53% of the ultimate tensile strength of the base phase, and the lowest strength is situated in the central fusion zone; 2) because of the excessive evaporation of elemental Zn and the significant inverse segregation of elemental Cu in cenral fusion welds, the major strengthening elements gather near the heat-affected zone; 3) the elastic modulus of hybrid welds is slightly larger than that of their base alloys, probably as a result of the inhomogeneity in their chemical composition, microstructure, geometry, and residual stress; 4) the pore size ranges from below 0.01 μm to approximately 107 μm, and it is modeled by the Schwartz-Saltykov method to reveal its damaging effects on the static strength; 5) a strength model of 7075-T6 welded butt joints is established to correlate with the elastic modulus, porosity, and heat inputs, and it coincides well with the computational and experimental results; and 6) in principle, the porosity has little influence on the static strength of hybrid welds, and the modified strengthening structure markedly dominates the overall mechanical properties.

Introduction

Age-hardened Al-Zn-Mg-Cu alloys, especially 7075 with T6 temper (7075-T6), have become some of the most widely used structural materials in the aerospace, high-speed train, and automotive industries because of their attractive mechanical properties (Ref. 1). Nonetheless, the high heat sensitivity and low eutectic liquidus temperature range of 7075-T6 make it difficult to weld with conventional arc welding methods. Hybrid laser arc welding (termed hybrid welding) was proposed to achieve a sound joint in both strength and geometry (Ref. 2). However, the welding process readily degrades the characteristics of the precipitation strengthening. This phenomenon has been observed to accompany a dramatic loss of static strength, although the strength can be partially recovered by elaborately designing the postweld aging (Refs. 3, 4). Prior studies have shown that heat-induced softening is primarily caused by the intrinsic dissolution and growth of precipitates (Refs. 5, 6). To prevent quality loss in 7075-T6 joints, solid-state friction stir welding (FSW) is being actively pursued as a potential alternative to fusion welding. Unfortunately, the softening behavior of the weld nugget zone (WNZ) and thermomechanically affected zone (TMAZ) remains a major challenge (Refs. 7, 8). Therefore, it is vital to deeply explore the softening mechanism of fusion hybrid welds.

Physically, the softening can be attributed to three causes. First, the strengthening elements, such as zinc, magnesium, copper, and their hybrids (intermetallic compounds) in the 7075-T6 matrix tend to be rearranged during welding, and this redistribution affects the microstructure and strength (Ref. 9). Previous papers have mainly focused on the evolution of precipitation phases in the base metals (Refs. 10–12), and a number of empirical models have been established to correlate the strength with the precipitates, aging stage, and compositions (Refs. 13, 14). Furthermore, the presence of various gas pores decreases the effective load capacity and has a detrimental effect on the mechanical properties. The relevant literature has paid more attention to the source, prevention, and formation of gas porosity (Ref. 15), and few works have reported the influence of this porosity on the static strength (Refs. 16, 17). This lack of information exists because it is difficult to detect the exact size, morphology, and distribution of pores in the fusion welded joints. Microcracks, inclusions, segregations, tensile residual stress, and filler metal (FM) are also responsible for the compromised mechanical properties (Ref. 18).

The softening that arises from these foregoing factors can seriously undermine the fitness for service of welded aluminum alloy structures (Ref. 19), in addition to deteriorating their load-carrying capacity, especially under variable reversed loads (Ref. 20). The existing literature has rarely

KEYWORDS

7075-T6 Aluminum Alloys
Hybrid Laser Arc Welding
Softening Behavior
Gas Porosity
Element Loss
Strength Modeling
Synchrotron Radiation X-Rays

S. C. WU (wushengchan@gmail.com) and, W. H. ZHANG are with State Key Lab of Traction Power, Southwest Jiaotong University, Chengdu, China. X. YU, R. Z. ZUO, and J. Z. JIANG are with School of Materials Science and Engineering, Hefei University of Technology, Hefei, China. H. L. XIE is with Shanghai Syncrotron Radiation Facility, Shanghai Institute of Applied Physics, Shanghai, China.

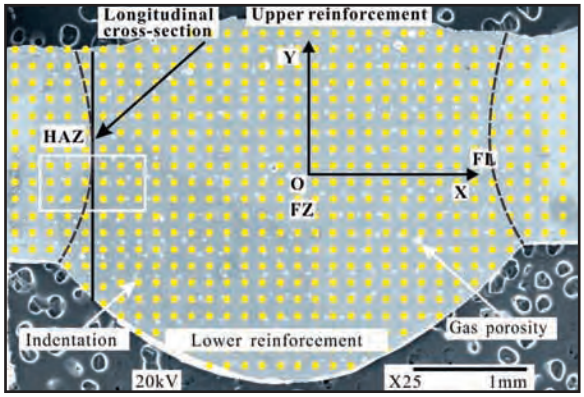

Fig. 1 — Typical SEM macroimage of the complete weld produced by hybrid laser arc welding, in which solid circles on the transverse cross section of the hybrid joint were used to illustrate the indentation points for the microhardness and white rectangle across the left weld interface was drawn to show triangular or polygonal particles. The black solid line near left-curved weld interface was actually the longitudinal cross plane as perpendicular to the x-y plane for the particle analysis by SEM. The z-axis is normal to the transverse cross section.

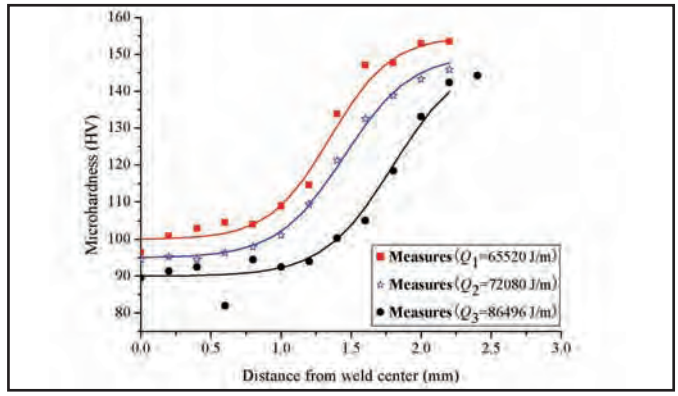

Fig. 2 — Microhardness distribution curves for hybrid welded 7075-T6 aluminum joints after 10 months' natural aging under different heat inputs: low heat input Q_1 = 65520 J/m, medium heat put Q_2 = 72080 J/m, and high heat input Q_3 = 86496 J/m.

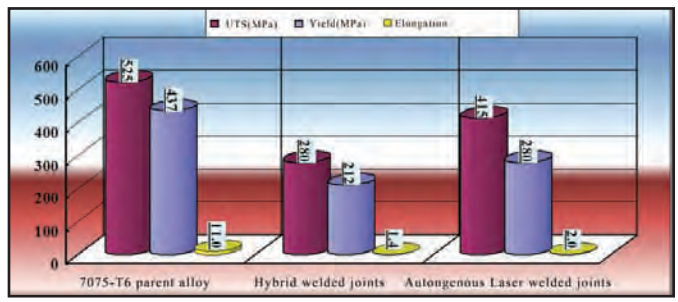

Fig. 3 — Yield strength, ultimate tensile strength, and elongation results from cross-tensile tests with the same gauge length of 10 mm on received base metal, hybrid welded joints after three months of natural aging, and autogenous laser welded joints after seven months of natural aging.

been concerned about the softening of hybrid welded 7075-T6 joints. Consequently, it is commercially and academically important to quantify the softening behavior of hybrid welded joints.

This work presents novel elemental composition and gas porosity results, and their roles in the strength of 7075-T6 butt joints are identified by measurements taken using the high-resolution Shanghai Synchrotron Radiation Facility (SSRF) (Ref. 21). The elemental composition and pores were detected using synchrotron radiation micro X-ray fluorescence (SR-μXRF) at the 15U beam line (BL15U) and synchrotron radiation X-ray microtomography (SR-XRM) at the 13W beam line (BL13W), respectively. Relatively perfect joints were obtained using hybrid welding, and nonheat-treatable ER5356 was used as the FM. A quantitative relationship between the strength with the porosity in hybrid welds was established based on the elastic modulus, heat input, and gas porosity. New insights are provided to characterize the heat-induced softening behaviors, which are expected to be an important complement to the recognition of the softening mechanism of hybrid fusion welded Al-Zn-Mg-Cu joints.

Experimental

Materials

Table 1 shows the chemical compositions of the high-strength 7075-T6 aluminum alloys and the self-developed consumable ER5356 (Φ1.2 mm) with yield strength of 120 MPa and ultimate tensile strength (UTS) of 260 MPa. A commercial 7075-T6 sheet was sheared into sample sizes of 240 × 60 × 2 mm^3. Following degreasing and abrading, the butting surfaces were carefully cleaned using a sodium hydroxide solution at 60°C. The samples were then washed in a dilute nitric acid solution. To reduce the hydrogen gas porosity as much as possible, both the BM and FM were placed into a dry, clear, well-ventilated storage space for no more than 24 h.

Hybrid Welding

Hybrid welding was performed by incorporating a fiber laser (YLR-4000) with a gas metal arc welding (GMAW, Fronius TPS4000) power source. The parameters of the laser were as follows: 0.4-mm focus spot diameter, 10 kW/mm^2 maximum output power density, 1.06-μm wavelength, and 150-mm focal length of the lens. The filler tip was 3 mm away from the laser axis, and 99.999% pure argon gas with a flow rate of 45 L/min was selected as the shielding gas. To alleviate reflection, the laser was inclined by approximately 10 deg, and the arc torch was inclined to the sample plane at a 70-deg angle. To prevent any relative movement, the plates were fixed onto a worktable using parallel slat clamps. Single-pass, butt-joint hybrid keyhole welding was then performed in the rolling direction.

For a good quality of butt joints, a large number of hybrid welding experiments were conducted, and the suitable parameters were as follows: P_{laser} = 2.5~3 kW laser power, I_{GMAW} = 90~110 A arc current, about U_{GMAW} = 23 V arc voltage, v_{torch}=2.5~3 m/min torch travel speed, v_{filler}= 5.3 m/min for the FM, and Δ = –1 mm defocusing distance. η_{laser} = 0.60 and η_{GMAW}=0.82 were thermal efficiency for the laser and GMAW heat source, respectively, and the heat input was $Q = (\eta_{laser} \cdot P_{laser} + \eta_{GMAW} \cdot I_{GMAW} \cdot U_{GMAW})/v_{torch}$.

Performance Examination

Briefly, the microstructure was investigated using an optical microscope (OM) and a scanning electron microscope (SEM). The morphology and distribution of the heat-induced particles were then examined near the heat-affected zone (HAZ).

Table 1 — Measured Nominal Chemical Composition (wt-%) of the 7075-T6 High-Strength Aluminum Alloy and the Self-Developed ER5356 Filler Metal

Elements	Zn	Mg	Cu	Ti	Mn	Cr	Fe	Si	Al
7075-T6	5.54	2.43	1.30	0.05	0.10	0.19	0.25	0.20	Bal.
ER5356	0.10	4.80	0.10	0.12	0.15	0.10	0.40	0.25	Bal.

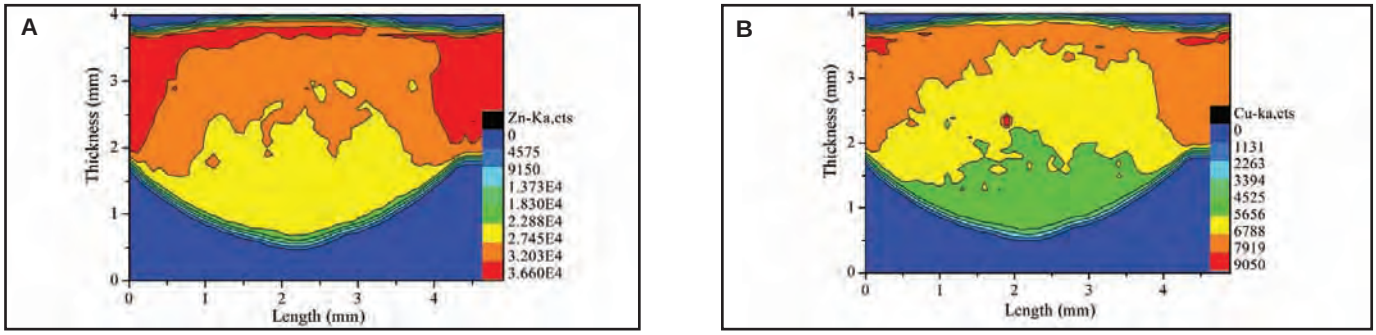

Fig. 4 — μXRF maps of elements Zn and Cu inside hybrid welded 7075-T6 joints after five months' natural aging for the case of high heat input Q_3=86496 J/m, in which 20-keV synchrotron radiation micro X-ray fluorescence was used at the 15U beam line. A — Element Zn; B — element Cu. Scale bars represent normal XRF intensity for the respective element.

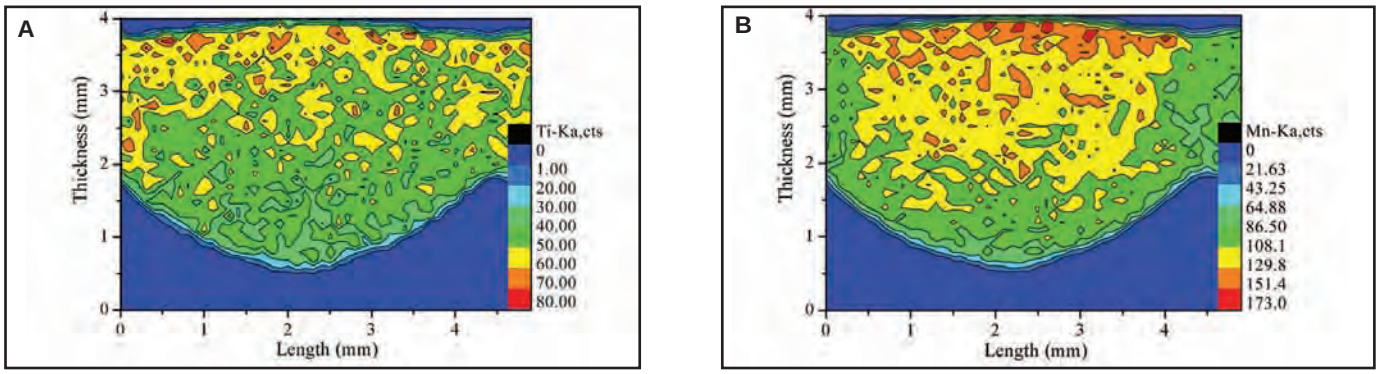

Fig. 5 — μXRF maps of elements Ti and Mn inside hybrid welded 7075-T6 joints after five months' natural aging for the case of high heat input Q_3=86496 J/m, in which 20-keV synchrotron radiation micro X-ray fluorescence was used at the 15U beam line. A — Element Ti; B — element Mn. Scale bars represent normal XRF intensity for the respective element.

Cross-tensile tests were conducted with hybrid and autogenous laser welded joints that had been naturally aged for three and seven months, respectively. The samples were machined to a 10-mm gauge length with a 25-mm width based on welded joint tensile test code (ISO 4136: 2001). The facility employed was an MTS 809 servohydraulic testing system with a load capacity of ±250 kN. The fractured surfaces were then examined for the fracture mode and distribution of gas pores and microcracks using SEM.

To obtain the hardness, the Vickers microhardness was examined along the transverse section with a load of 200 g for approximately 10 s. The natural aging period was 10 months for present hybrid welded joints. Figure 1 demonstrates the spatial distribution of the pressed points in a complete joint.

Synchrotron Radiation X-Ray

The strengthening elements were mapped in the sectioned welds with a synchrotron radiation light source. The high flux and low divergence of the SR-μXRD demonstrate its advantage in quantifying alloying elements with less damage to the irradiated samples (Refs. 22, 23). The samples were ground and polished to a 1.5-mm thickness, and a maximum energy of 20 keV was selected to ensure a 30% transmission rate. The spot size was 1.6 × 1.8 μm^2 inside the sample with a focus photon flux density of 1.8×10^{11} phs/(s·μm^2) at 10 keV. The fluorescent intensities were measured using a liquid-nitrogen-cooled seven-element energy-dispersive high-purity Si(Li) detector, and the sample was scanned in the "step-by-step" mode at BL15U. Using this method, it took a total time of 1.5 h to pick up a total of 10,000 pixels. Unfortunately, the strengthening elemental Mg could not be detected because of its absorption edge limit.

The formation of pores is a problem when joining 7075-T6. Complete avoidance of pores is unrealistic for fusion welding. High-resolution SR-XRM has become the most advanced tool (Ref. 24) to determine the exact descriptions of the gas pores, as well as their size, morphology, position, number, and distribution (Ref. 25). A voxel size of 0.7 μm was chosen as the sample size, representing a compromise between the minimum size of the gas pores and the 2048 × 2048 CCD detector. Successive two-dimensional (2D) in situ slices were obtained at BL13W, and these slices were subsequently reconstructed using the Amira software for three-dimensional (3D) images.

It is vital to evaluate the influence of the pores on the mechanical properties. Many methods have been introduced to determine the 3D size distribution of spherical pores. Here, the classical Schwartz-Saltykov (SS) method is selected because it is suitable to the zero-continuity and low fraction of the pores (Refs. 26, 27). By characterizing the gas porosity, the damage to the static strength can be evaluated.

Results and Discussion

Softening Behavior

Figure 2 shows the hardness distribution curves along the x-axis illustrated in Fig. 1, for three cases of welding heat inputs Q_1 = 65520 J/m, Q_2 = 72080 J/m, and Q_3 = 86496 J/m. It is clearly observed that the welding heat input has a primary effect on the hardness. A higher heat input results in a larger softening region, a relatively wider fusion zone (FZ), and a lower hardness (Ref. 28). Moreover, it was also found that the hardness changes slowly from the joint center to the weld interface (WI) and then increases suddenly to the level of base metal (BM). The hardness profiles fully show that the welded joint is mechanically and compositionally heterogeneous, which practically makes the FZ the weakest part of the aluminum welded structures.

To clearly reveal the serious softening behavior of hybrid welded joints, cross-tensile tests with a 25-mm gauge length were conducted for the BM and two types of welded joints. Tensile results show that almost all fractures occurred near the PMZ rather than the central FZ. It is seen in Fig.

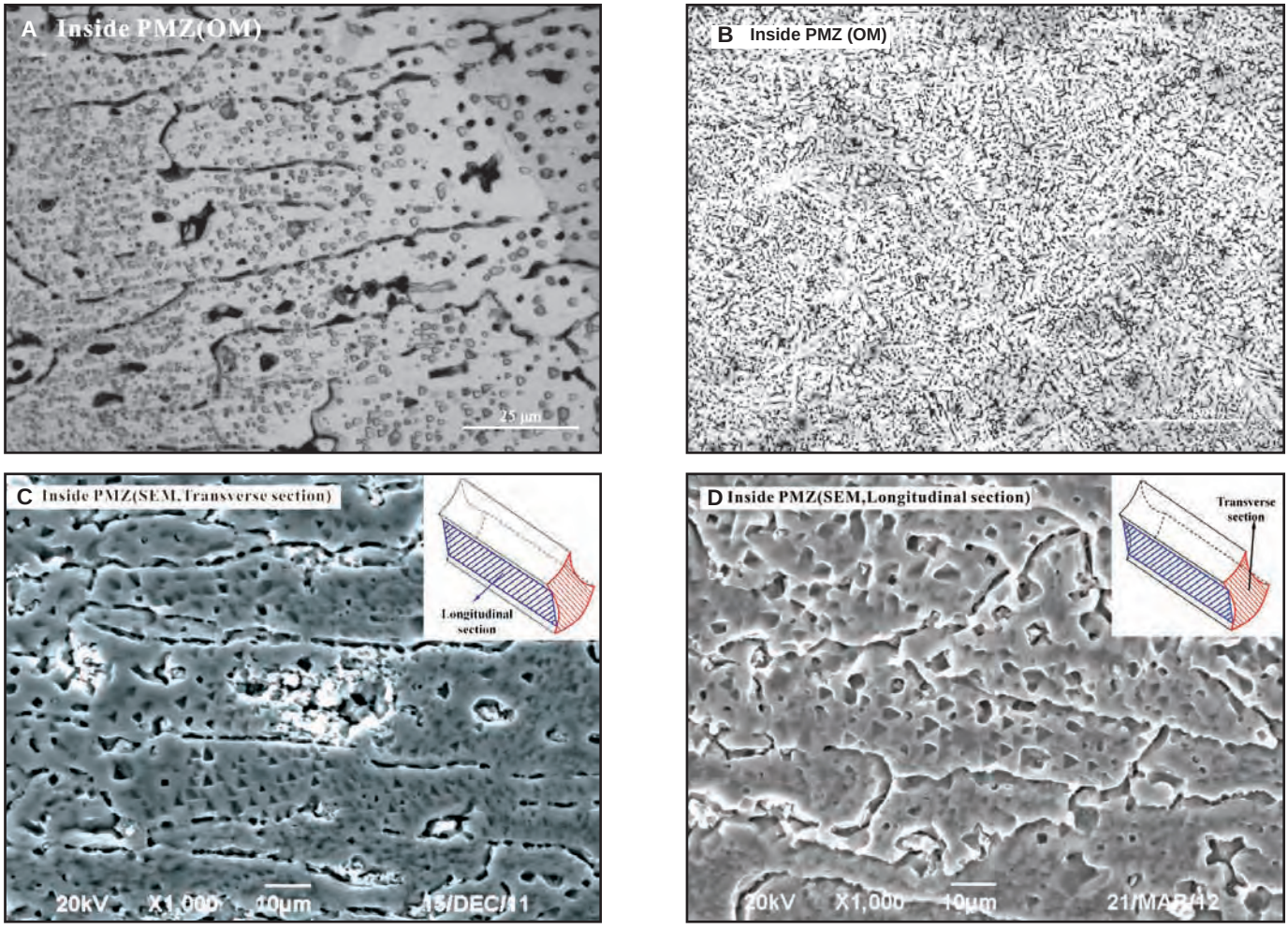

Fig. 6 — Optical microscope images of the following: A — PMZ (×1000); B — central FZ microstructures with slightly etched hybrid welded metallographic specimen after 17 months' natural aging. Scanning electron microscope micrographs of the following: C — Transverse cross section or oxy *plane PMZ microstructures; D — PMZ microstructures of the longitudinal cross section as illustrated in Fig. 1 or the plane parallel to* oyz *with slightly etched hybrid welded metallographic specimen after 10 and 11 months' natural aging, respectively.*

3 that the hybrid joints achieve the lowest yield strength and UTS that is only approximately 53% of the strength of the base 7075-T6 material, indicating serious softening. In contrast, autogenous laser welds obtain a slightly higher UTS because of the lower heat input.

Elemental Mapping

It is known that the 7075-T6 alloy achieves its high strength from a series of precipitates such as typical $\eta(MgZn_2)$ and $T(Al_2Mg_3Zn)$ (Refs. 29, 30). The content and gradient of the alloying elements change distinctly in hybrid welds and play a primary role in the microstructure and resulting properties. Few studies have examined the softening mechanism from the elemental perspective. Figure 4 shows the spatial distribution of the major Zn and Cu strengthening elements. The elemental mappings are graded using a continuous color bar. Each bar is assigned to an elemental level, for which red is the highest, yellow is medium, and blue is the lowest.

It can be observed that Zn and Cu have similar distributions, and their concentration is lowest near the lower reinforcement and highest near the HAZ. It is generally thought that owing to the excessive energy accumulation during welding, less Zn is found in the FZ because of its low boiling point. While inverse segregation happens for the strengthening element Cu, that is to say, the region that solidifies first has the higher Cu (Ref. 31). The element-induced softening appears to be consistent with the hardness variation seen in Fig. 2. The relationship and mechanism between the change of alloying elements such as Cu and Zn with the mechanical performance of welded joints were not explored in present research mainly due to limited information. However, one important point should be noted that the biggest effect of element variation would come from the filler dilution. In other words, the main contribution to the lower content of Zn and Cu is probably the addition of ER5356 FM into the molten pool.

Ti and Mn are usually considered impurities in commercial 7075-T6 aluminum alloys. Nevertheless, they sometimes play useful roles in either refining grains or forming dispersed second phases of $MnAl_6$ and $(Cr,Mn)Al_{12}$. A small amount of elemental Ti in ER5356 helps to form $TiAl_3$ dispersion particles smaller than 0.5 μm and refine the weld microstructure. As a dispersed precipitate, elemental Mn is effective in preventing the grain growth (Ref. 32). Figure 5 shows the distribution maps of Ti and Mn.

The map shows that Ti and Mn exhibit a comparable distribution. The top region of the weld has a slightly higher content, and a lower content in the lower reinforcement.

The level of Zn is the highest of all other elements, which is consistent with the alloying contents listed in Table 1. Elemental Ni and Co are also identified by the 20-keV synchrotron micro X-ray spectrums. No further qualitative efforts are made to analyze these results.

Microstructure

The strength and hardness of welded joints always depend on the elemental redistribution and microstructural changes

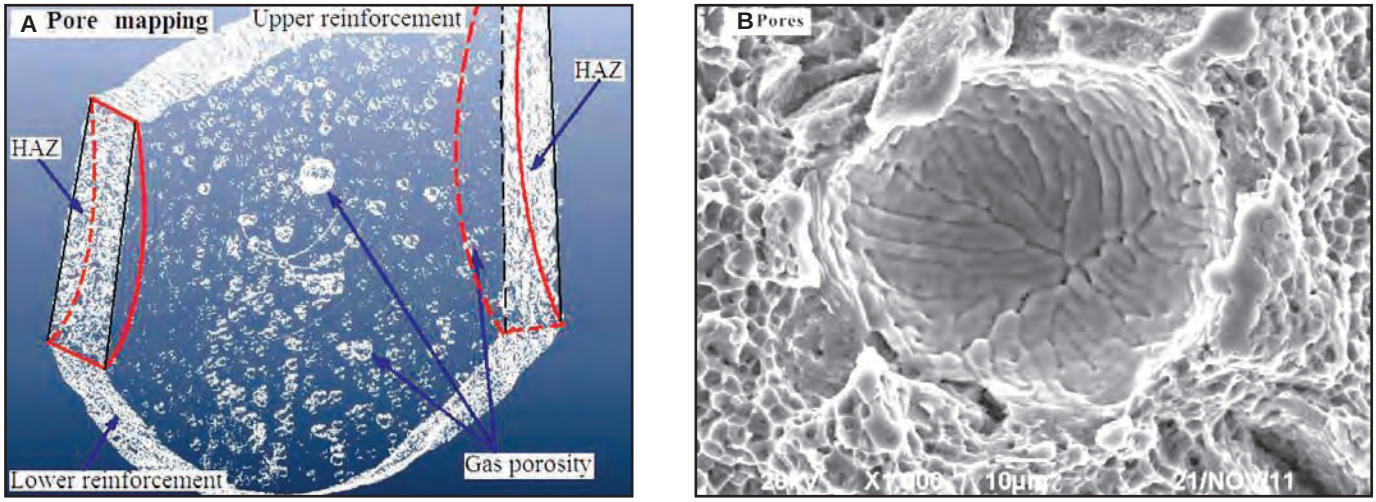

Fig. 7 — X-ray microtomography mapping of 3D porosity with detailed size, amount, distribution, morphology, and location inside the hybrid 7075-T6 weld with 40-keV synchrotron radiation XRM at the 13W beam line and SEM fracture morphology micrograph of typical gas porosity under low heat input $Q_1 = 65520$ *J/m.*

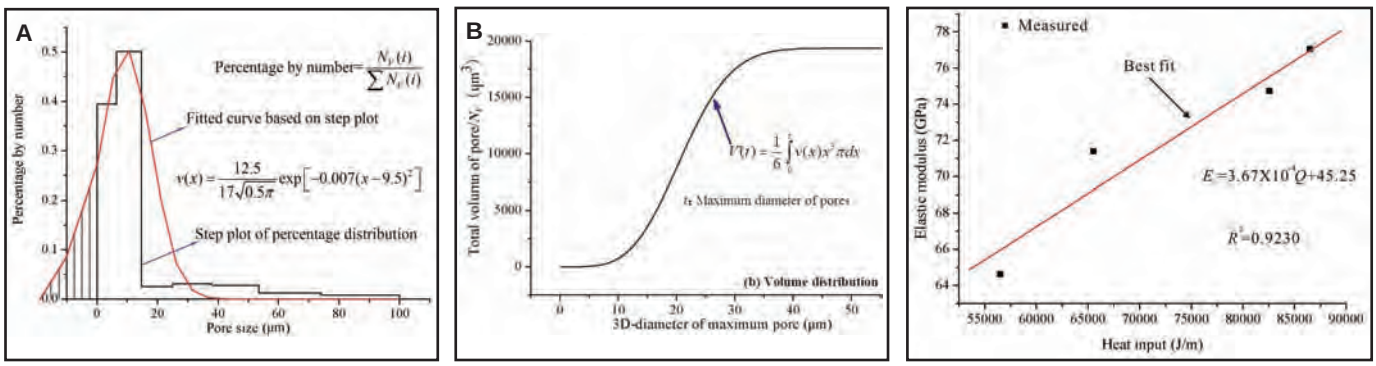

Fig. 8 — Size and volume distributions of 3D pore size in hybrid 7075-T6 welds derived by the Schwartz-Saltykov analysis according to the diameters variation $[D_{max}\times 10^{-0.1(i-2)} \sim D_{max}\times 10^{-0.1(i-1)}]$. *A — The relationship between percentage by number; B — the correlation of maximum volume* V′(t) *and maximum diameter* t.

Fig. 9 — The curve that is fit to the relationship between elastic modulus E_s *and heat input* Q *of hybrid welded 7075-T6 aluminum joints measured from the cross-tensile tests.*

Table 2 — The Number of Gas Pores in Each Volume Interval and Resulting Maximum Volume

Interval	Porosity diameter (μm)	3D porosity	Maximum volume (μm^3)
$i=1$	99.90~74.04	1	1.25×10^7
$i=2$	74.04~53.49	2	8.50×10^6
$i=3$	53.49~37.90	7	7.05×10^6
$i=4$	37.90~24.93	8	2.74×10^6
$i=5$	24.93~14.64	7	6.49×10^5
$i=6$	14.65~6.48	289	2.59×10^5
$i=7$	6.48~0.01	184	1.77×10^5

that occur when the weld experiences an intense thermal history. Figure 6 illustrates the OM and SEM images of two mutual vertical sections denoted in Fig. 1. These images show the typical solidification characteristics of columnar dendritic structures near the HAZ and equiaxed dendritic structures in the central FZ together with the morphology of particles inside the partially melted zone (PMZ, about 100 μm width) near the WI.

Figure 6A shows the coarse grains containing a large number of dispersed particles near the PMZ of the transverse cross section. These particles appear as equilateral triangles and polygons with the size varied from 0.1 to 2.5 μm when slightly etched using Keller's reagent. Figure 6C shows their morphology more clearly under SEM. These types of precipitates gradually increase from either side of the PMZ and few were found in both the central FZ and BM. Further studies show that these precipitates contain a large amount of Zn and a little Fe, which is basically consistent with the elemental mappings seen in Fig. 4. Thorough information concerning the chemical compositions of precipitated phases and their influence on the mechanical properties will be investigated in another work.

The FZ exhibits finely equiaxed dendritic structures, as seen in Fig. 6B, which are attributed to the higher cooling rate. The lower hardness is most likely caused by the eutectic constituent precipitates or the disappearance of the Guinier-Preston (GP) zone (Ref. 33). It should be specially noted that the FM also makes a pronounced contribution to the strength of welds due to its dilution effect of composition.

Figure 6D further shows the morphology of particles in the longitudinal cross section running through the PMZ. It is basically concluded that these particles exhibit some kind of typical spatial shape. It is of value to explore the detailed information of composition, microstructure, and resulting performance.

Modeling Porosity

The previous sections briefly discuss the softening mechanism from the perspective of the hardness, strength, and elemental composition, which is mainly responsible for the lower strength and hardness. The gas pores formed during hybrid welding present another problem that contributes to the loss of mechanical behavior of hybrid 7075-T6 welds.

Figure 7 shows a stereogram of the gas

porosity and fractured surface inside a weld. Many voids and microcracks were observed surrounding the pores, which might be related to the isolated particles on the dendrite boundary. However, the voids and microcracks are treated as pores for convenience and simplification. Voids and microcracks can act with gas pores under loading, affecting the performance and life of the material as a whole (Refs. 34, 35).

According to the SS approach, the number of 3D pores is represented as n volume intervals of $N_V(i)$, where $i=1,2\ldots n$, and the diameters are $[D_{max}\times10^{-0.1(i-2)}\sim D_{max}\times10^{-0.1(i-1)}]$ for the ith interval, where D_{max} is the diameter of the largest 3D pore (Ref. 36). Table 2 lists the volume distribution of the gas pores shown in Fig. 7.

The 3D size distribution of the total porosity can be readily derived, and the best-fit curve for the size was created as a function of the step plot of percentage, as shown in Fig. 8A.

Special attention should be paid to the negative number of pores in the 3D size distribution, which is primarily caused by inherent cumulative error (Ref. 37). Based on the fitted function of $v(x)$, the correlation of the maximum volume $V'(t)$ and maximum diameter t can be established as shown in Fig. 8B. The total pore volume $V(t)$ can be calculated using the product $Nv\cdot V'(t)$. Thus, the porosity $p(t)$ of the hybrid welds under a set of suitable welding parameters is simply expressed as follows:

$$p(t)=V(t)/V=N_v\cdot V'(t)/V \qquad (1)$$

where V is the volume of the specified welds. It is assumed that V is solely related to the welding parameters instead of the size of the pores. It is suggested that a longer weld pool results in a lower porosity inside the welded joints.

Two assumptions are made to correlate the total porosity $p(t)$ with the effective heat input ($Q=(\eta_1P_1+\eta_2P_2)/v$, where η_1 and η_2 are the energy efficiencies of the laser and arc heat source, respectively; P_1 and P_2 are the total output laser power and arc heat source power; and v is the welding speed): $V=a_1Q$, and $N_V=a_2\tau$, where a_1 and a_2 are undetermined constants, and τ is the total retention time of weld pool. By substituting these equations into Equation 1, the following alternative relationship can be obtained:

$$p(t)=cQ^{-2}V'(t) \qquad (2)$$

where c is an undetermined constant related to the welding process.

It can be clearly seen that Q not only can trigger the elemental redistribution in welds, but it can also drive the production of gas pores and voids. Therefore, the welding heat input Q is the principal factor that determines the mechanical properties of welded joints. The following section is focused on the detailed quantification of this relationship between the tensile strength with the heat input Q and the porosity $p(t)$.

Table 3 — Computed Mechanical Properties of the Hybrid 7075-T6 Welds Based on Strength Model of Hybrid Welds

Q (J/m)	E_m (GPa)	σ_m (MPa)	σ_m/σ_p (%)	σ_d (MPa)	σ_d/σ_p (%)
Q_1	70.18	266.68	50.79	517.98	98.64
Q_2	72.43	275.23	52.42	519.14	98.86
Q_3	77.49	294.46	56.08	521.01	99.22
Mean	73.37	278.79	53.10	519.38	98.91

Table 4 — Predicted Properties of the Hybrid 7075-T6 Welds

Q (J/m)	$\sigma_{s(p)}$ (MPa)	Error (%)	Weakening (%)
Q_1	259.56	–0.46	49.43
Q_2	269.27	–0.12	51.28
Q_3	290.37	0.39	55.30

Strength Model

Different models have been established to nondestructively determine the mechanical properties of commercial Al-Zn-Mg-Cu alloys (Refs. 38–41). However, little research has been published on the relationship of the strength to variations in the strengthening alloying elements, porosity, and welding heat inputs.

Elastic Modulus-Tensile Strength Relationship

In the present formulation, the true stress-strain responses of the 7075-T6 alloy and its hybrid welded joints are assumed to obey similar exponential functions; therefore, the offset yield strength $\sigma_{0.2}$ at $\varepsilon=0.002$ is

$$\sigma_{0.2}=B(0.002)^n \qquad (3)$$

$$\sigma_{0.2}=0.002E \qquad (4)$$

where B and n are the strength coefficient and the hardening parameter, respectively.

At the uniaxial UTS, the differential of the load P is zero, which gives an analytical relationship between the tensile strength σ and the spot area A in the form of $-dA/A=d\sigma/\sigma$ when necking occurs. Additionally, the volume constraint gives the correlation $dL/L=dA/A$, where L is the specimen length. Then the strain at the necking point ε_b can be obtained as follows:

$$\varepsilon_b=n \qquad (5)$$

Based on the strain energy theory at a given strain, σ is

$$\sigma=Bn^n/1+n \qquad (6)$$

The relationship of the tensile strength σ with the elastic modulus E is given by

$$\sigma/E=n^n/(1+n)\cdot0.002^{n-1} \qquad (7)$$

Modeling Weld Strength

The mechanical properties of engineering materials are generally determined by their chemical composition and microstructure, but the properties are also sensitive to various macro- and microdiscontinuities. Gas porosity is considered to be this type of damage. Therefore, we can establish a strength model by dividing the overall property into two main parts: one part arises from the metallurgical aspect in the absence of discontinuity, and the other arises only from microdamage, including gas porosity, voids, microcracks, and inclusions, in the absence of metallurgical modification of the structures and elements. Therefore, the elastic modulus can be rewritten as follows:

$$E_d/E_p=[(1-p(t))]^2 \qquad (8)$$

where E_d is the corresponding measure of weld flaws induced by gas pores, and E_p is the value of the BM. Thus, the practical elastic modulus E_s is expanded as follows:

$$E_s=E_p+(E_d/E_p-1)E_p+(E_m/E_p-1)E_p \qquad (9)$$

where E_m is the contribution of the microstructure in terms of chemical composition, and E_s can be measured through tensile tests, as shown in Fig. 9.

The correlation coefficient (R^2, with a value of 0.9230) suggests a good correlation between the measured E_s with the given heat inputs. By incorporating Equations 7–9 and establishing a best-fit equation, we can obtain the following:

$$\frac{E_m}{E_p}=\frac{E_s}{E_p}+1-\left[1-p(t)\right]^2$$

$$=\frac{E_s}{E_p}+1-\left[1-cQ^{-2}V'(t)\right]^2 \qquad (10)$$

If Equation 7 is applied to the microstructure-induced strength, the gas porosity-induced strength of the welds, and base 7075-T6 materials, the practical tensile strength can eventually be expressed as follows:

$$\sigma_s=\sigma_p-(\sigma_p-\sigma_m)-(\sigma_p-\sigma_d) \quad (11)$$

Verification of Strength Model

To verify the proposed strength model, three sets of hybrid laser arc welds were conducted. The corresponding porosity $p(t)$ from Equation 1, the maximum gas pore diameter t, and the measured ultimate strength $\sigma_{s(m)}$ were conveniently acquired. For the first heat input Q_1, $p_1(t)=0.0117$, $t_1=102$ μm, and $\sigma_{s1(m)}=260.77$ MPa. For the second heat input Q_2, $p_2(t)=0.0038$, $t_2=84$ μm, and $\sigma_{s2(m)}=269.60$ MPa. For the third heat input Q_3, $p_3(t)=0.0024$, $t_3=107$ μm, and $\sigma_{s3(m)}=289.23$ MPa. The UTS of the BM is $\sigma_p=525.10$ MPa, and this UTS corresponds to $E_p=66.21$ GPa. By substituting the data from the above three cases into Equation 2, the corresponding constants can be obtained: $c_1=2589.00$, $c_2=1017.68$, and $c_3=925.55$. As a result, the mean constant is $c=1510.74$.

Based on this empirical constant c, we can expediently predict the porosities for the three heat inputs: $p_1(t)=0.0068$, $p_2(t)=0.0056$, and $p_3(t)=0.0039$. Finally, we can compute the mechanical strengths of the welded joints by combining Equations 7 and 8 with 10, in which the hardening parameter n is 0.18 for the welded 7075-T6 joints. Table 3 lists the calculated data for E_m, σ_m, and σ_d.

The alloying-element-induced microstructure plays the dominant role in defining the static properties of hybrid welds, compared with porosity-induced discontinuities. In other words, the essential change of the strengthening phases inside the welds produces the softening behavior. However, the mechanical performances of the welds are sensitive to internal discontinuities, such as gas pores, voids, microcracks, inclusions, segregations, and impurities when undergoing reversed loading and unloading (Refs. 42–44).

By using the experimental data from Table 3, the practical ultimate tensile strength $\sigma_{s(p)}$ and softening behavior can easily be predicted in terms of the computed UTS, as given in Table 4.

It is apparent that the predicted material performance agrees with the experimental results, which validates the proposed strength model in terms of the elements and porosities, as analyzed from SR-μXRF and SR-XRM, respectively.

There is a nearly linear relationship between the elastic modulus and heat input for the hybrid welds, compared to that of the base 7075-T6 material. It is thought that the inhomogeneity and complex residual stress leads to greater stiffness. This type of asymmetry might be visible from the weld geometry, mechanical properties, chemical composition, and microstructure. Furthermore, the discontinuities resulted from the microcracks are susceptible to significant stress concentrations, which easily generate localized yield zones, even when the load level is small.

It would be of interest to clarify the following issues in the future. First, the mechanism of the larger elastic modulus of welded joints is not clear and requires further metallurgical proof and characterization. Second, the composition and structure parameters of the newly observed phases or particles should be identified, characterized, and related to the complex mechanical behaviors inside the PMZ near the HAZ. Finally, the accumulated elemental Zn and Cu might correlate with the evolution of the strengthening phases and microsegregations, formation of hot cracks, and variation of the hardness. Relevant results will be presented in subsequent research.

Conclusions

This paper systematically reports a new quantitative perspective on the softening behavior of hybrid 7075-T6 butt joints. Significant physical softening is observed as a steep loss in hardness and strength as a result of the welding process. Elements and gas pores in the welds are measured using SR-μXRF and SR-XRM, respectively. A new strength model is then formulated and validated using the experimental results. From the present study, the following conclusions are obtained:

1. The heat input has great influence on the strength loss due to welding. A greater heat input produces a wider softening region, a wider FZ, and, thus, a lower hardness. The FZ has the lowest hardness at approximately 95 HV, which produces a notable decrease in mechanical properties. This trend is consistent with the strength variation in terms of the UTS.

2. The strengthening elements Zn and Cu change dramatically inside the hybrid 7075-T6 welds. The HAZ contains the maximum content, and the minimum is found in the center of the FZ. Because of its higher melting temperature, Zn evaporates rapidly, whereas less Cu collects in the FZ probably because of inverse segregation. It is generally thought that the dilution of FM plays a pronounced effect on the redistribution of strengthening elements.

3. There are a great number of unknown grown precipitates found inside the columnar dendritic grain on the PMZ with about 100 μm width. Either side of the PMZ has few such triangular particles whose size varies from 0.1 to 2.5 μm. These precipitated phases contain a large amount of Zn and a little Fe.

4. The largest size of the metallurgical pores varies from 0.1 to 0.2 mm. The formulated porosity, $p(t)=cQ^{-2}V'(t)$, was found to be proportional to the negative square of the heat input and maximum diameter of the gas pores.

5. The microstructure-induced strength without discontinuity and porosity-induced strength without structural changes are treated independently to establish a new strength model. It is found that this model is in agreement with the experimental data from the heat inputs and porosity.

6. The predicted results show that the porosity-induced strength loss has little influence on the overall strength of the 7075-T6 joints, whereas the variation in element-induced microstructures dominates the strength.

7. The elastic modulus of the hybrid welds is greater than that of the base 7075-T6 aluminum material. Additionally, the elastic modulus appears to linearly increase with the increase in the heat input.

Acknowledgments

Financial support from the National Nature Science Foundation of China (Grant No. 51005068), the National Basic Research Program of China (973 Program, Grant No. 2011CB 711105-1) and the Open Research Fund Program of the State Key Lab of Advanced Design and Manufacturing for Vehicle Body (Grant No.: 31115030) is gratefully acknowledged.

References

1. Williams, J. C., and Stark Jr., E. A. 2003. *Acta. Mater.* 51: 5775.
2. Staufer, H. 2007. Laser hybrid welding in the automotive industry. *Welding Journal* 86(10): 36.
3. Nelson, T. W., Steel, R. J., and Arbegast, W. J. 2003. *Sci. Technol. Weld. Joi* 8: 283.
4. Hu, B., and Richardson, I. M. 2007. *Mat Sci. Eng. A* 459: 94.
5. Dorward, R. C. 1999. *Mater. Sci. Tech.* 15: 1133.
6. Deschamps, A., Ringeval, S., Texier, G., and Delfaut-Durut, L. 2009. *Mat. Sci. Eng. A* 517: 361.
7. Fratini, L., Buffa, G., and Shivpuri, R. 2010. *Acta. Mater.* 58: 2056.
8. Steuwer, A., Dumont, M., Altenkirch, J., Birosca, S., Deschamps, A., Prangnell, P. B., and Withers, P. J. 2011. *Acta. Mater.* 59: 3002.
9. Cho, W. I., Na, S. J., Cho, M. H., and Lee, J. S. 2010. *Comput. Mater. Sci.* 49: 792.
10. Ringer, S. P., and Hono, K. 2000. *Mater. Character.* 44: 101.
11. Liu, M., Klobes, B., and Maier, K. 2011. *Scripta. Mater.* 64: 21.
12. Buha, J., Lumley, R. N., and Crosky, A.

G. 2008. *Mat. Sci. Eng. A* 492: 1.
13. Gang, S., and Cerezo, A. 2004. *Surf Interface Anal.* 36: 564.
14. Werenskiold, J C., Deschamps, A., and Brechet, Y. 2000. *Mat. Sci. Eng. A* 293: 267.
15. Zhou, J., and Tsai, H. L. 2007. *J. Heat Trans-T* ASME 129: 1014.
16. Pastor, M., Zhao, H., Martukanitz, R. P., and DebRoy, T. 1999. Underfill and magnesium loss during continuous-wave Nd:YAG laser welding of thin plates of aluminum Alloys 5182 and 57 porosity. *Welding Journal* 78(6): 207.
17. Phillion, A. B., Cockcroft, S. L., and Lee, P. D. 2008. *Mat. Sci. Eng. A* 491: 237.
18. Wu, Y. E., and Wang, Y. T. 2010. *J. Mater. Eng. Perform.* 19: 1362.
19. Rodrigues, D. M., Menezes, L. F., and Loureiro, A. 2004. *Eng. Fract. Mech.* 71: 2053.
20. Zhang, H., Toda, H., Qu, P. C., Sakaguchi, Y., Kobayashi, M., Uesugi, K., and Suzuki, Y. 2009. *Acta Mater* 57: 3287.
21. Cyranoski, D. 2009. *Nature* 459: 16.
22. Rosenbaum, G., Holmes, K. C., and Mitz, J. 1971. *Nature* 230: 434.
23. Rao, D. V., Swapna, M., Cesareo, R., Brunetti, A., Akatsuka, T., Yuasa, T., Takeda, T., Tromba, G., and Gigante, G. E. 2009. *J. Trace. Elem. Med. Bio.* 23: 251.
24. Baruchel, J., Buffiere, J. Y., Cloetens, P., Michiel, M. D., Ferrie, E., Ludwig, W., Maire, E., and Salvo, L. 2006. *Scripta. Mater.* 55: 41.
25. Rack, A., Helwig, H. M., Butow, A., Rueda, A., Matijasevic-Lux, B., Helfen, L., Goebbels, J., and Banhart, J. 2009. *Acta. Mater.* 57: 4809.
26. Saltykov, S. A. 1976. *Stereometric Metallography*, third ed. Moscow: Metallurgiya.
27. Shen, H., Oppenheimer, S. M., Dunand, D. C., and Brinson, L. C. 2006. *Mech. Mater.* 38: 933.
28. Ma, T., and Ouden, G. D. 1999. *Mat Sci Eng. A* 266: 198.
29. Davis, J. R. 1993. *Aluminum and Aluminum Alloys*. Materials Park, Ohio: ASM International.
30. Zhou, J., Zhao, S. Q., and Li, X. C. 2010. *Microstructure and Metallography of Aluminum Alloys*. Beijing: Metallurgical Industry Press (in Chinese).
31. Zhang, B. J., Cui, J. Z., and Lu, G. M. 2003. *Mater. Lett.* 57: 1707.
32. Nagaumi, H., Suzuki, S., Okane, T., Umeda, T. 2008. *Mater. Trans.* 49: 324.
33. Cai, B., Adams, B. L., and Nelson, T. W. 2007. *Acta. Mater.* 55: 1543.
34. Morgeneyer, T. F., Starink, M. J., and Sinclair, I. 2008. *Acta. Mater.* 56: 1671.
35. Maire, E., Grenier, J. C., Daniel, D., Baldacci, A., Klocker, H., and Bigot, A. 2006. *Scripta. Mater.* 55: 123.
36 Susan, D. 2005. *Metall. Mater. Trans. A* 36: 2481.
37. Liu, Y., German, R. M., and Iacocca, R. G. 1999. *Acta. Mater.* 47: 915.
38. Rudy, J. F. and Rupert, E. J. 1970. Effects of porosity on mechanical properties of aluminum welds. *Welding Journal* 49: 322.
39. Kamp, N., Sinclair, I., and Starink, M. J. 2002. *Metall. Mater. Trans. A* 33: 1125.
40. Starink, M. J., and Wang, S. C. 2003. *Acta. Mater.* 51: 5131.
41. Dumont, D., Deschamps, A., and Brechet, Y. 2003. *Mat. Sci. Eng. A* 356: 326.
42. Gao, Y. X., Yi, J. Z., Lee, P. D., and Lindley, T. C. 2004. *Acta Mater* 52: 5425.
43. Lefebvre, F., and Sinclair, I. 2005. *Mat. Sci. Eng. A* 407: 265.
44. Xue, Y., Kadiri, H. E., Horstemeyer, M. F., Jordon, J. B., and Weiland, H. 2007. *Acta. Mater.* 55: 1975.

Authors: Submit Research Papers Online

Peer review of research papers is now managed through an online system using Editorial Manager software. Papers can be submitted into the system directly from the *Welding Journal* page on the AWS Web site (*www.aws.org*) by clicking on "submit papers." You can also access the new site directly at *www.editorialmanager.com/wj/*. Follow the instructions to register or log in. This online system streamlines the review process, and makes it easier to submit papers and track their progress. By publishing in the *Welding Journal*, more than 69,000 members will receive the results of your research.

Additionally, your full paper is posted on the American Welding Society Web site for FREE access around the globe. There are no page charges, and articles are published in full color. By far, the most people, at the least cost, will recognize your research when you publish in the world-respected *Welding Journal*.

Looking for a Welding Job?

The American Welding Society has enhanced its Jobs In Welding Web site at *www.jobsinwelding.com*.

The redesigned career portal includes additional capabilities for companies seeking workers and individuals looking for jobs.

Through relationships with many job boards and distributors, it offers direct access to more than 88% of the welding-related jobs posted on the Internet.

Users may search various openings for welders, Certified Welding Inspectors, engineers, technicians, and managers/supervisors.

In addition, the Web site contains the following highlights:

- The home page displays featured welding jobs along with the companies looking to fill them and city/state locations.
- The job seeker section connects individuals to new career opportunities by allowing them to post an anonymous résumé, view jobs, and make personal job alerts. This area has résumé tips, certification information, and a school locator.
- The employer area enables association with qualified applicants. Résumés, job postings, and products/pricing options may be viewed here.

Visit the Web site to create or access job seeker and employer accounts.